

# Uncertainty-Guided Coarse-to-Fine Tumor Segmentation with Anatomy-Aware Post-Processing

Ilkin Sevgi Isler

Department of Computer Science  
University of Central Florida  
Orlando, FL, USA  
ilkin@ucf.edu

David Mohaisen

Department of Computer Science  
University of Central Florida  
Orlando, FL, USA  
mohaisen@ucf.edu

Curtis Lisle

KnowledgeVis  
LLC  
Altamonte Springs, FL, USA  
clisle@knowledgevis.com

Damla Turgut

Department of Computer Science  
University of Central Florida  
Orlando, FL, USA  
damla.turgut@ucf.edu

Ulas Bagci

Department of Radiology  
Northwestern University  
Chicago, IL, USA  
ulas.bagci@northwestern.edu

**Abstract**—Reliable tumor segmentation in thoracic computed tomography (CT) remains challenging due to boundary ambiguity, class imbalance, and anatomical variability. We propose an uncertainty-guided, coarse-to-fine segmentation framework that combines full-volume tumor localization with refined region-of-interest (ROI) segmentation, enhanced by anatomically aware post-processing. The first-stage model generates a coarse prediction, followed by anatomically informed filtering based on lung overlap, proximity to lung surfaces, and component size. The resulting ROIs are segmented by a second-stage model trained with uncertainty-aware loss functions to improve accuracy and boundary calibration in ambiguous regions. Experiments on private and public datasets demonstrate improvements in Dice and Hausdorff scores, with fewer false positives and enhanced spatial interpretability. These results highlight the value of combining uncertainty modeling and anatomical priors in cascaded segmentation pipelines for robust and clinically meaningful tumor delineation. On the Orlando dataset, our framework improved Swin UNETR Dice from 0.4690 to 0.6447. Reduction in spurious components was strongly correlated with segmentation gains (HD95:  $\rho = -0.83$ ,  $p < 0.0001$ ), underscoring the value of anatomically informed post-processing.

**Index Terms**—uncertainty, tumor segmentation, lung cancer,

## I. INTRODUCTION

The accurate and reliable segmentation of lung tumors in computed tomography (CT) images remains a persistent challenge in thoracic oncology and medical image analysis [1]. Performance often suffers due to tumor heterogeneity, class imbalance, partial volume effects, and boundary ambiguity caused by both intra- and inter-patient variation [2]. These issues are particularly acute near the pleura, mediastinum, and central hilar regions, where tumors may cross anatomical

Dr. Bagci acknowledges the following grants: NIH R01-CA240639, and FDOH (Florida Department of Health) through the James and Esther King Biomedical Research Program-20K04

boundaries or exhibit indistinct contours [3]. While most gross tumor volumes (GTVs) reside within the lung parenchyma, a clinically important subset partially extends beyond the lung walls [4]. This makes it difficult to rely on rigid anatomical priors such as lung-only masking [5].

Despite advances in deep learning-based segmentation, few models transition into clinical workflows. A key barrier is the lack of interpretability and error awareness in deterministic systems. Clinical integration requires more than high Dice scores; it demands spatial reliability, manageable false positives, and transparency in uncertain regions [6]. This highlights the need for segmentation frameworks that incorporate uncertainty modeling and anatomical reasoning not as optional features, but as essential elements for clinical deployment [7].

**Our Contribution and Findings.** To address these needs, we propose a two-stage, end-to-end segmentation framework that combines coarse tumor localization with refined region-of-interest (ROI) segmentation. In the first stage, a full-volume model identifies candidate tumor regions. These are refined through a clinically informed post-processing pipeline that applies anatomical constraints, including lung overlap thresholds, minimum surface distance, and region-specific filters. Rather than introducing an explicit localization model, we treat segmentation as a surrogate for localization. We show that lightweight, anatomy-aware post-processing can yield high spatial fidelity without increasing computational load.

We also show that reducing the number of candidate components passed to the second-stage model improves both segmentation accuracy and predictive confidence. This supports the view that component selection functions as a form of spatial attention. Focusing on the most salient regions enhances robustness, especially in challenging cases. These improvements are achieved without added architectural com-

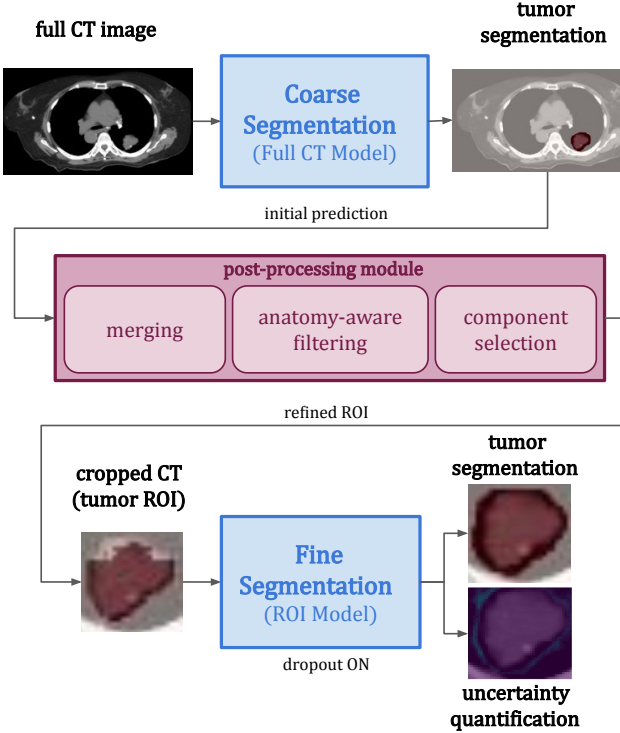


Fig. 1. Overview of the proposed two-stage tumor segmentation framework. The first-stage model performs coarse segmentation on the full CT scan and outputs both a tumor prediction and an uncertainty map. Post-processing—including edge enhancement, lung masking, and ROI cropping—uses these outputs to generate a refined input region. The second-stage model conducts fine segmentation on the cropped ROI to produce the final tumor mask. The uncertainty map enhances interpretability and supports adaptive refinement around ambiguous boundaries.

plexity, underscoring the effectiveness of domain-informed filtering over brute-force model scaling.

In the second stage, the model incorporates uncertainty-aware loss functions to adaptively optimize predictions in high-ambiguity areas, particularly at tumor boundaries. This uncertainty modeling enhances spatial calibration and provides interpretable outputs, offering clinicians an additional layer of review that can strengthen confidence in the results.

We evaluate the framework through a series of experiments that examine the influence of ROI context, component count, and uncertainty-driven training objectives. The results demonstrate that the proposed anatomy-aware, uncertainty-refined segmentation system achieves competitive accuracy while improving interpretability and clinical plausibility. These findings advance the practical utility of automated tumor segmentation in thoracic imaging.

**Organization.** The rest of this paper is organized as follows. In section II we review the related work. In section III, we present our methodology, including dataset and preprocessing, our two-stage segmentation framework, component selection strategy, and uncertainty-aware loss function with model architecture and post-processing. In section IV we present our results and analysis, followed by conclusion in section V.

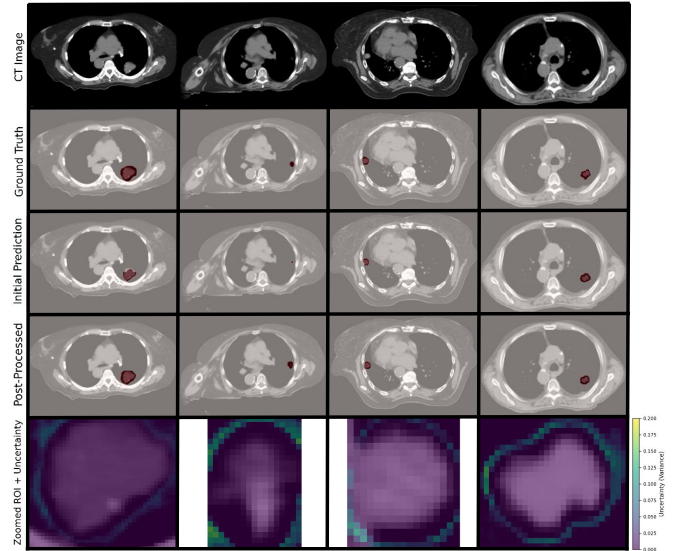


Fig. 2. Example patient cases from our proposed two-stage segmentation pipeline. From left to right: full CT image, ground truth mask, initial prediction, post-processed prediction, and the region-of-interest (ROI) prediction with uncertainty map overlay. Our pipeline demonstrates improved tumor delineation and spatial accuracy through uncertainty modeling and anatomical post-processing.

## II. RELATED WORK

There have been several studies related to this work, focusing on lung tumor segmentation, region-of-interest learning, uncertainty-aware segmentation, anatomically informed post-processing, and considerations for clinical translation, which we review in the following.

**Lung Tumor Segmentation.** Deep learning-based methods have significantly advanced lung tumor segmentation in CT, with architectures such as U-Net [8] and its 3D extensions becoming foundational, producing state-of-the-art results. Variants like UNETR [9] and Swin UNETR [10] leverage transformer-based encoders for better global context understanding. However, segmenting tumors that are small, irregular, or located near anatomical boundaries remains challenging due to class imbalance and limited spatial cues.

**Region-of-Interest (ROI) Learning.** Cascade segmentation approaches decompose the problem into coarse localization followed by fine segmentation, often improving accuracy while reducing computational cost [5]. Prior work has explored tight cropping [11] or context-aware padding [12] to balance precision and spatial understanding. Our work adopts a similar strategy but incorporates domain-specific post-processing to enhance ROI selection reliability.

**Uncertainty-Aware Segmentation.** Uncertainty modeling has emerged as a powerful tool for enhancing model interpretability in medical imaging with multiple competing results [13]. Techniques such as Monte Carlo dropout [14], test-time augmentation [15], and ensemble methods [16] allow quantification of predictive variance. These approaches support adaptive learning and improve robustness, particularly in ambiguous

regions. Recent work introduced MC-Swin-U [17], a self-supervised transformer model that integrates Monte Carlo dropout for voxel-wise uncertainty estimation in lung tumor and organ-at-risk segmentation. We build upon this foundation by integrating uncertainty into the ROI model’s loss function to focus optimization on high-ambiguity areas.

**Anatomically Informed Post-Processing.** Several studies apply anatomical priors to filter out implausible predictions. For example, lung masking [18] and anatomical constraints based on spatial location or proximity to lung surfaces have been used to reduce false positives [19]. Our method extends this idea through a multi-criteria filtering scheme that incorporates lung overlap thresholds, distance-based heuristics, and component size criteria to ensure that only clinically plausible regions are refined in the second stage.

**Clinical Translation Considerations.** Despite high Dice scores in the experimental settings, many segmentation systems fail in clinical deployment due to the lack of interpretability and error awareness [20]. As such, recent trends emphasized the need for pipelines that offer spatial reliability, explainability, and robustness to distribution shift [21]. To this end, our approach addresses these needs by combining spatial filtering, ROI segmentation, and uncertainty quantification in a modular, interpretable framework.

### III. METHODOLOGY

This study proposes a two-stage, end-to-end segmentation framework that integrates coarse tumor localization, uncertainty-aware ROI refinement, and anatomically guided post-processing. The goal is to enhance segmentation precision, robustness, and interpretability in thoracic CT scans while maintaining computational efficiency. The methodology is structured to evaluate segmentation performance under variations in ROI context, component selection, uncertainty modeling, model architecture, and dataset generalization.

#### A. Datasets and Preprocessing

This study utilizes two datasets for training and evaluation. The primary dataset consists of thoracic CT scans collected from a private institutional source, with expert-annotated tumor segmentation. Due to institutional privacy restrictions, this dataset is not publicly available but serves as the foundation for model development and internal validation. To assess generalization, the proposed pipeline was replicated on the publicly available NSCLC-Radiomics dataset using the same experimental configuration, enabling reproducibility and comparative analysis across domains.

All CT scans were resampled to an isotropic resolution and intensity-normalized to a fixed window prior to model input. Lung masks were generated using a pre-trained lung segmentation model and applied during post-processing.

The same pre-processing, ROI extraction, and component selection procedures were used for both datasets to ensure consistency. This unified pipeline enables the evaluation of segmentation accuracy, model robustness, and uncertainty

calibration under real-world variability and cross-institutional generalizability, which are ideal for systemic evaluation.

#### B. Two-Stage (Cascade) Segmentation Framework

The proposed pipeline follows a coarse-to-fine, cascade segmentation architecture designed to decompose the tumor segmentation task into two sub-problems: (1) coarse localization and (2) boundary refinement.

**Stage 1 (Coarse Localization):** The full-resolution CT volume is processed by a 3D segmentation model to generate a coarse tumor prediction map. This stage operates deterministically, without dropout or uncertainty modeling. Connected component analysis is then applied to the binary prediction to extract candidate regions for further refinement.

**Stage 2 (ROI-Based Refinement):** A configurable number of top- $k$  candidate components are selected based on the initial prediction map. These components are then cropped and passed to a second-stage model trained for high-resolution segmentation. Two region-of-interest (ROI) extraction strategies are employed to balance precision and context. The first, referred to as ROI-0margin, uses tight crops around each component’s bounding box. The second, ROI-16margin, extends each bounding box by 16 voxels in all directions to include the surrounding anatomical context, aiding in segmenting ambiguous or irregular boundaries.

This two-stage framework allows the model to concentrate computation on spatially relevant regions, reducing class imbalance and background noise. Anatomical priors, in the form of lung masks, are used to exclude regions outside the pulmonary space from being forwarded to the second stage.

#### C. Component Selection Strategy

Component selection is treated as a spatial focusing mechanism within the proposed framework. After the initial coarse segmentation stage, connected components are extracted from the predicted tumor mask based on their voxel volume. To control the complexity and relevance of the regions passed to the second-stage model, three selection strategies are evaluated: retaining only the single largest component (**Top-1**), selecting the two largest components (**Top-2**), or preserving all components that exceed a predefined minimum volume threshold (**All Valid**). This filtering serves as a form of implicit attention, guiding the model to concentrate on the most prominent tumor candidates while suppressing low-confidence or anatomically implausible regions. Empirically, reducing the number of components not only improves segmentation accuracy but also correlates with reduced uncertainty in the final predictions—highlighting the effectiveness of component selection as both a denoising and uncertainty attenuation step.

#### D. Uncertainty-Aware Loss Functions

Uncertainty modeling is applied exclusively in the second-stage ROI models, which are trained using both a baseline Dice-plus-cross-entropy loss and an uncertainty-aware adaptive loss to assess the benefits of ambiguity-sensitive learning. The baseline loss uses a fixed-weight combination of Dice

loss and binary cross-entropy. In contrast, the uncertainty-guided adaptive loss dynamically scales pixel-wise contributions based on estimated uncertainty. This is formulated as:

$$\mathcal{L}_{\text{adaptive}} = \alpha(x) \cdot \mathcal{L}_{\text{Dice}} + (1 - \alpha(x)) \cdot \mathcal{L}_{\text{CE}}, \quad \alpha(x) = \exp(-U(x)),$$

where  $U(x)$  represents the uncertainty at pixel  $x$ , computed from the variance of multiple stochastic forward passes using Monte Carlo (MC) Dropout. To support this, dropout layers remain active during inference, enabling the generation of variance-based uncertainty maps that inform both loss reweighting during training and interpretability during evaluation.

#### E. Model Architectures

To evaluate the sensitivity of the proposed framework to architectural variations, multiple 3D segmentation backbones—UNet, UNETR, and Swin UNETR—were integrated into the end-to-end pipeline. A baseline model was trained on full-resolution CT volumes using a single-stage approach, serving as a reference for comparison.

In contrast, the ROI-based segmentation models were trained on region-of-interest (ROI) crops extracted using either tight bounding (0-margin) or padded context (16-margin). Each model was evaluated under different loss configurations, including both standard and uncertainty-aware objectives.

All networks were implemented using the MONAI framework and trained with the Adam optimizer, cosine learning rate scheduling, and a range of spatial and intensity augmentations. Pretrained encoder weights, obtained from a dataset of 5,000 CT scans, were used when available to accelerate convergence and improve feature generalization [10].

#### F. Post-Processing

Post-processing was applied exclusively to the outputs of the first-stage coarse segmentation model to refine tumor candidate regions before ROI extraction. This stage ensures that only anatomically plausible and spatially relevant regions are passed to the second-stage model, reducing false positives, improving ROI focus, and contributing to lower predictive uncertainty by filtering out ambiguous or anatomically inconsistent candidates. The refinement process involved a series of spatial filters informed by clinical and anatomical knowledge, which we review in the following:

- 1) **Component Merging via Dilation.** Binary dilation using a 3D kernel was applied to the predicted tumor mask to merge closely adjacent or fragmented regions. This step addresses partial connectivity issues in coarse predictions and ensures that neighboring tumor clusters are treated as single components when appropriate.
- 2) **Lung Overlap Filtering.** Each connected component was evaluated based on its volumetric overlap with a binary lung mask. Components with low overlap (e.g.,  $< 80\%$ ) were generally discarded. However, rigid filtering is not appropriate for certain clinical cases, such as tumors that extend into the pleura or chest wall, so a more nuanced

TABLE I  
COMPARISON OF THE ORIGINAL MODEL VS. THE PROPOSED END-TO-END SYSTEM USING TOP-1 ROI. WE COMPARE TWO ROI MODELS TRAINED ON DIFFERENT SETTINGS (ROI-0MARGIN AND ROI-16MARGIN).

System	Dice Score	HD95 (mm)
Original Full CT	0.469	187.97
End-to-End (Top-1, ROI-16margin model)	0.5917	10.79
End-to-End (Top-1, ROI-0margin model)	0.6447	8.89

TABLE II  
EFFECT OF THE NUMBER OF COMPONENTS USED DURING INFERENCE. WE EVALUATE THE END-TO-END SYSTEM PERFORMANCE USING TOP-1, TOP-2, AND ALL VALID COMPONENTS AFTER POST-PROCESSING.

ROI Components Used	Dice Score	HD95 (mm)
Top 1	0.6447	8.89
Top 2	0.6082	73.65
All Valid Components	0.6010	85.13

rule was applied. Stricter overlap thresholds were enforced for components located in the central mediastinal zone, where false positives are more likely due to the surrounding anatomical complexity.

- 3) **Distance to Lung Surface.** Some valid tumors, particularly those located peripherally, may partially reside outside the lung mask while remaining anatomically adjacent to the lung. To avoid excluding such plausible candidates, components with low overlap were retained if their minimum distance to the lung boundary was below a defined threshold (e.g.,  $\leq 5$  voxels) and their size exceeded a minimum voxel count. This approach captures borderline tumors that are anatomically consistent despite limited lung intersection.
- 4) **Top-K Component Selection (Optional).** After filtering, the  $K$  largest components by voxel volume were optionally retained to reduce clutter and improve focus. This can be interpreted as a form of spatial attention, guiding the second-stage model to prioritize the most prominent tumor candidates while suppressing ambiguous or minor regions. These post-processing heuristics reflect common clinical scenarios. While most gross tumor volumes (GTVs) lie within the lung parenchyma and are well-captured by lung masks, tumors may also extend into extrapulmonary areas such as the pleura or mediastinum. The pipeline is therefore designed not only to suppress anatomically implausible predictions but also to preserve clinically relevant yet spatially borderline tumors that may extend beyond lung boundaries. By filtering for structural plausibility and emphasizing dominant components, the post-processing step enhances the quality of ROI extraction and reduces noise in the downstream fine segmentation stage.

## IV. RESULTS AND COMPARATIVE ANALYSIS

Performance was evaluated using Dice Score, 95th percentile Hausdorff Distance (HD95), and, where applicable, the Boundary Dice Coefficient. The following analysis examines

TABLE III

IMPACT OF COMPONENT REDUCTION ON SEGMENTATION PERFORMANCE. GROUPED STATISTICS SHOW AVERAGE DICE AND HD95 BASED ON A NUMBER OF CONNECTED COMPONENTS, WHILE CORRELATION METRICS QUANTIFY THE RELATIONSHIP BETWEEN COMPONENT REDUCTION AND PERFORMANCE IMPROVEMENTS.

Grouping / Metric	Avg. Dice Score	Avg. HD95 Score
1 Component	0.5750	7.5333
3+ Components	0.4513	10.0933
Pearson Correlation	-0.55 (p = 0.021)	-0.69 (p = 0.0021)
Spearman Correlation	-0.50 (p = 0.040)	-0.83 (p < 0.0001)

TABLE IV

EFFECT OF USING DIFFERENT LUNG MASKS IN THE END-TO-END SYSTEM. WE COMPARE THE ORIGINAL LUNG MASK WITH A NEWLY GENERATED ONE.

Lung Mask Used	Dice Score	HD95 (mm)
Original Lung Mask	0.6467	8.89
New Lung Mask	0.6447	8.89

the effects of ROI refinement, component filtering, post-processing heuristics, and uncertainty-aware training.

**Two-Stage vs. Baseline.** The two-stage framework was first compared to a baseline single-stage full-volume segmentation model. As shown in Table I, both ROI-0margin and ROI-16margin configurations outperformed the baseline. The ROI-0margin setup achieved the highest Dice score (0.6447) and lowest HD95 (8.89 mm), indicating that tighter cropping yields more accurate segmentation.

**Impact of Component Selection.** Table II reports the results on the impact of component selection. We found that retaining only the largest component (Top-1) led to the best results, and including additional components (Top-2 or All Valid) reduced Dice and increased HD95, suggesting that false positives and irrelevant regions impair segmentation.

**Component Count Correlation Trends.** Component count trends are shown in Table III. We found that cases with a single connected component exhibited consistently higher Dice scores (0.5750) and lower HD95 values (7.53) compared to those with three or more components (Dice = 0.4513, HD95 = 10.09). Moreover, the statistical analysis further supports this trend: the reduction in component count was significantly correlated with the segmentation improvement, with a Pearson correlation of  $r = -0.55$  ( $p = 0.021$ ) for the Dice and  $r = -0.69$  ( $p = 0.0021$ ) for the HD95 scores. A strong Spearman correlation was also observed for HD95 reduction ( $\rho = -0.83$ ,  $p < 0.0001$ ), suggesting a robust monotonic relationship. These findings confirm that anatomical and uncertainty-informed postprocessing not only simplifies segmentation output but also enhances overall accuracy.

**Lung Mask Quality Comparison.** The lung mask quality was evaluated, and the results are shown in Table IV, comparing the LungMask library [18], auto-generated masks, and human-annotated ground truth. HD95 was similar across methods, while Dice improved only slightly with manual annotations.

TABLE V

IMPACT OF USING AN UNCERTAINTY-AWARE LOSS FUNCTION IN THE ROI MODEL. ALL MODELS ARE EVALUATED IN AN END-TO-END SETUP USING TOP-1 ROI.

ROI Model	Dice Score	HD95 (mm)
Standard S4 ROI Model	0.6447	8.89
S4 ROI with Uncertainty-Aware Loss	0.6321	8.92

TABLE VI

PERFORMANCE COMPARISON OF FOUR SEGMENTATION MODELS ON ORLANDO HEALTH AND NSCLC DATASETS USING TOP-1 ROI AND UNCERTAINTY-AWARE LOSS. DICE AND HD95 METRICS ARE REPORTED FOR BOTH INITIAL AND IMPROVED VERSIONS.

Model	Dice (Init)	Dice (Imp)
<i>Orlando Health Dataset</i>		
UNet (K=1)	0.3136	0.4415
UNetR (K=1)	0.3018	0.4281
SwinUNetR (K=1)	0.469	0.6447
<i>NSCLC Dataset</i>		
UNet	0.3737	0.4605
UNetR	0.5258	0.5602
SwinUNetR	0.4731	0.4860

This supports the use of the LungMask library as a reliable tool for lung segmentation without requiring expert input.

**Uncertainty-Aware Loss Evaluation.** Table V presents the results of an ablation study on uncertainty-aware loss. While the standard Dice Cross-Entropy loss achieved marginally better Dice and HD95, the uncertainty-guided variant improved spatial calibration and boundary interpretability, which are important for clinical review.

**Cross-Model Performance Comparison.** Cross-architecture and cross-dataset results using Top-1 component selection and uncertainty-aware loss are also studied and summarized in Table VI. On the Orlando Health dataset, Swin UNETR achieved the highest performance gain, improving from 0.4690 to 0.6447. UNET and UNETR also showed substantial gains, but from lower baselines. These results indicate that models with better initial segmentation enable more effective localization and refinement, which is expected.

**NSCLC Dataset Performance Trends.** On the NSCLC dataset, all models improved with the two-stage pipeline. UNET increased from 0.3737 to 0.4605, UNETR from 0.5258 to 0.5602, and Swin UNETR from 0.4731 to 0.4860. While the overall trend remains consistent—better base models yield stronger performance—the improvements were smaller than on the Orlando dataset. Notably, Swin UNETR did not show the largest gain here, suggesting that initial model quality is a factor but not the sole determinant of refinement effectiveness.

**Loss Impact on Accuracy.** Finally, Table VII compares the performance of different loss functions. Dice Cross-Entropy achieved the highest Dice, lowest HD95, and best boundary accuracy. Among uncertainty-aware methods, the Uncertainty-Weighted Lovász loss was the most competitive, reflecting a trade-off between robustness and interpretability.

TABLE VII

TUMOR SEGMENTATION PERFORMANCE ACROSS LOSS FUNCTIONS (ROI-BASED EVALUATION).

Loss Function	Dice $\uparrow$	HD95 $\downarrow$	Boundary Dice $\uparrow$
Uncertainty-Aware	0.789	5.349	0.492
Distance Transform	0.777	5.027	0.464
U-W Lovász	0.792	4.809	0.469
Dice CE	<b>0.799</b>	<b>4.696</b>	<b>0.503</b>

**Summary of Key Findings.** The proposed two-stage segmentation framework significantly outperformed the baseline single-stage approach, particularly when using tightly cropped ROI inputs. The use of Top-1 component selection led to higher accuracy and reduced boundary errors, while including additional components introduced false positives and degraded performance. A clear negative correlation was observed between the number of components and segmentation quality, highlighting the value of post-processing. Moreover, lung mask quality had little effect, affirming the reliability of automated segmentation. While standard Dice Cross-Entropy loss yielded the best metrics, uncertainty-aware objectives enhanced spatial calibration and interpretability, key for clinical use. Swin UNETR showed the greatest improvement on the Orlando dataset, with more modest gains on NSCLC, indicating that initial model quality affects but does not fully determine refinement success. Overall, the results highlight the complementary value of ROI refinement, component filtering, and uncertainty modeling for accurate, clinically meaningful tumor segmentation.

## V. CONCLUSION

This study demonstrates the effectiveness of a two-stage, anatomy-aware segmentation framework for tumor delineation in lung CT. By combining ROI refinement, component filtering, and post-processing heuristics, the proposed approach significantly improves segmentation accuracy and reliability. Cases with fewer connected components exhibited higher Dice scores and lower HD95 values, with statistically significant correlations confirming the relationship between component reduction and performance improvement.

Across both the Orlando Health and NSCLC datasets, ROI cropping and Top-1 component selection consistently outperformed baseline full-volume models. Although uncertainty-aware loss functions did not always yield higher Dice or HD95 scores, they enhanced spatial calibration and boundary consistency which are critical factors in clinical interpretation.

The integration of anatomical priors, lightweight postprocessing, and uncertainty modeling yields a robust and interpretable segmentation pipeline. These findings support the use of modular, post-hoc strategies to refine predictions from modern segmentation networks, especially in scenarios with limited supervision or heterogeneous imaging conditions.

## REFERENCES

[1] S. G. Armato III, G. McLennan, L. Bidaut, M. F. McNitt-Gray, C. R. Meyer, A. P. Reeves, B. Zhao *et al.*, “The lung image database consortium (lidc) and image database resource initiative (idri): a completed reference database of lung nodules on ct scans,” *Medical physics*, vol. 38, no. 2, pp. 915–931, 2011.

[2] Z. Zhou, M. M. R. Siddiquee, N. Tajbakhsh, and J. Liang, “Lung tumor segmentation with missing tumor labels,” *Medical Image Analysis*, vol. 64, p. 101713, 2020.

[3] Q. Tong, G. Song, C. Yang, and et al., “Fully automatic one-step segmentation of pulmonary tumors from multi-source heterogeneous ct imaging using deep convolutional neural networks,” *Physics in Medicine & Biology*, vol. 65, no. 22, p. 225010, 2020.

[4] H. Tang, Y. Xu, Y. Zhang, and et al., “Lung tumor segmentation on ct scans using boundary-aware neural networks,” *Medical Image Analysis*, vol. 75, p. 102307, 2022.

[5] F. Isensee, P. F. Jaeger, S. A. Kohl, J. Petersen, and K. H. Maier-Hein, “nnu-net: Self-adapting framework for u-net-based medical image segmentation,” in *Nature Methods*, vol. 18, no. 2, 2021, pp. 203–211.

[6] B. Kompa, J. Snoek, and A. L. Beam, “Second opinion needed: communicating uncertainty in medical machine learning,” *NPJ Digital Medicine*, vol. 4, no. 1, pp. 1–6, 2021.

[7] M. H. Hesamian, W. Jia, X. He, and P. Kennedy, “Deep learning techniques for medical image segmentation: achievements and challenges,” *Journal of Digital Imaging*, vol. 32, no. 4, pp. 582–596, 2019.

[8] O. Ronneberger, P. Fischer, and T. Brox, “U-net: Convolutional networks for biomedical image segmentation,” *International Conference on Medical Image Computing and Computer-Assisted Intervention (MICCAI)*, pp. 234–241, 2015.

[9] A. Hatamizadeh, V. Nath, Y. Tang, D. Yang, A. Myronenko, B. Landman, H. R. Roth, and D. Xu, “Unetr: Transformers for 3d medical image segmentation,” *IEEE/CVF Winter Conference on Applications of Computer Vision (WACV)*, pp. 574–584, 2022.

[10] Y. Tang, D. Yang, W. Li, H. R. Roth, B. Landman, D. Xu, V. Nath, and A. Hatamizadeh, “Self-supervised pre-training of swin transformers for 3d medical image analysis,” in *Proceedings of the IEEE/CVF conference on computer vision and pattern recognition*, 2022, pp. 20730–20740.

[11] X. Li, H. Chen, X. Qi, Q. Dou, C.-W. Fu, and P.-A. Heng, “H-denseunet: Hybrid densely connected unet for liver and tumor segmentation from ct volumes,” in *IEEE Transactions on Medical Imaging*, vol. 37, no. 12, 2018, pp. 2663–2674.

[12] Y. Zhou and et al., “Cascaded unet for kidney tumor segmentation,” in *MICCAI Kidney Tumor Segmentation Challenge (KiTS)*, 2019.

[13] A. Kendall and Y. Gal, “What uncertainties do we need in bayesian deep learning for computer vision?” *Advances in Neural Information Processing Systems (NeurIPS)*, vol. 30, 2017.

[14] Y. Gal and Z. Ghahramani, “Dropout as a bayesian approximation: Representing model uncertainty in deep learning,” in *International Conference on Machine Learning (ICML)*, 2016, pp. 1050–1059.

[15] G. Wang and et al., “Aleatoric uncertainty estimation with test-time augmentation for medical image segmentation with convolutional neural networks,” *Neurocomputing*, vol. 338, pp. 34–45, 2019.

[16] A. Mehrtash, W. M. Wells III, C. M. Tempany, P. Abolmaesumi, and T. Kapur, “Confidence calibration and predictive uncertainty estimation for deep medical image segmentation,” in *International Conference on Medical Image Computing and Computer-Assisted Intervention (MICCAI)*, 2020, pp. 676–685.

[17] I. Isler, D. Jha, C. Lisle, J. Rineer, P. Kelly, B. Aydogan, M. Abazeed, D. Turgut, and U. Bagci, “Self-supervised learning for organs at risk and tumor segmentation with uncertainty quantification,” in *2023 3rd International Conference on Electrical, Computer, Communications and Mechatronics Engineering (ICECCMEE)*. IEEE, 2023, pp. 1–6.

[18] J. Hofmanninger, F. Prayer, J. Pan, S. Röhricht, H. Prosch, and G. Langs, “Automatic lung segmentation in routine imaging is primarily a data diversity problem, not a methodology problem,” *European radiology experimental*, vol. 4, pp. 1–13, 2020.

[19] X. Yang, S. Sun, D. Liang, S. Zhang, and D. Feng, “Automatic liver and tumor segmentation of ct and mri volumes using cascaded fully convolutional neural networks,” in *arXiv preprint arXiv:1704.02703*, 2017.

[20] G. Litjens, T. Kooi, B. E. Bejnordi, A. A. A. Setio, F. Ciompi, M. Ghafoorian, J. A. van der Laak, B. van Ginneken, and C. I. Sánchez, “A survey on deep learning in medical image analysis,” *Medical Image Analysis*, vol. 42, pp. 60–88, 2017.

[21] A. Reinke and et al., “Common limitations of performance metrics in biomedical image analysis,” *Nature Communications*, vol. 12, no. 1, p. 6048, 2021.